

On the pore-scale mechanisms leading to brittle and ductile deformation behavior of crystalline rocks

Martin Tjioe and Ronaldo I. Borja^{*,†}

Department of Civil and Environmental Engineering, Stanford University, Stanford, CA 94305, U.S.A.

SUMMARY

Deformation mechanisms at the pore scale are responsible for producing large strains in porous rocks. They include cataclastic flow, dislocation creep, dynamic recrystallization, diffusive mass transfer, and grain boundary sliding, among others. In this paper, we focus on two dominant pore-scale mechanisms resulting from purely mechanical, isothermal loading: crystal plasticity and microfracturing. We examine the contributions of each mechanism to the overall behavior at a scale larger than the grains but smaller than the specimen, which is commonly referred to as the mesoscale. Crystal plasticity is assumed to occur as dislocations along the many crystallographic slip planes, whereas microfracturing entails slip and frictional sliding on microcracks. It is observed that under combined shear and tensile loading, microfracturing generates a softer response compared with crystal plasticity alone, which is attributed to slip weakening where the shear stress drops to a residual level determined by the frictional strength. For compressive loading, however, microfracturing produces a stiffer response than crystal plasticity because of the presence of frictional resistance on the slip surface. Behaviors under tensile, compressive, and shear loading invariably show that porosity plays a critical role in the initiation of the deformation mechanisms. Both crystal plasticity and microfracturing are observed to initiate at the peripheries of the pores, consistent with results of experimental studies. Copyright © 2015 John Wiley & Sons, Ltd.

Received 14 May 2014; Revised 16 December 2014; Accepted 23 December 2014

KEY WORDS: crystal plasticity; deformation mechanisms; finite element; heterogeneity; microfracture

1. INTRODUCTION

The response of porous rocks during mechanical loading is of relevance to many real-world applications. Depletion activities during hydrocarbon extraction may result in inelastic compaction that gives rise to ground surface subsidence, borehole instability, or triggered seismicity. Carbon sequestration, hydraulic fracturing applied to geothermal reservoirs and shale gas production, and numerous enhanced hydrocarbon recovery methods that rely on injecting fluids at elevated pressure may induce seismicity, brittle fractures, and faults [1–19].

An interesting phenomenological behavior of porous rocks lies in their failure mechanism, which transitions from brittle faulting to ductile flow. During brittle faulting, a macroscopic stress drop is observed after the peak stress has been achieved [20], whereas during ductile flow, the stress stays constant or continues to increase, albeit at a slower rate. Early experimental studies discovered that this transition takes place at the stress state when the frictional strength exceedance occurs at the same time as fracture creation [21, 22]. At low confining pressure, the rock typically fails through brittle faulting, but when the confining pressure is increased sufficiently, cataclastic flow occurs, and no stress drop is observed. Further studies have demonstrated that this transition stress state is also affected by the porosity of the rock [24, 25].

*Correspondence to: Ronaldo I. Borja, Department of Civil and Environmental Engineering, Stanford University, Stanford, CA 94305, U.S.A.

†E-mail: borja@stanford.edu

There have been a number of experimental studies investigating the micromechanics of quartzite, limestone, and sandstone. Both micritic and allochemical limestones have demonstrated that cataclasis is the dominant mechanism [26, 27]. Microcracks have been observed to originate from the pores, with the larger pores driving crack propagation. Cataclastic flow, which results in compactive behavior, has been observed to be transient, giving way to net dilatancy at a higher strain rate [23, 24]. However, experiments reported in the literature do not allow the individual deformation mechanisms to be isolated, and so the contributions of each mechanism cannot be quantified from the complex interaction of different mechanisms.

Discrete element models of rock's microstructure have been used with some success to model the brittle-ductile transition in rocks. These models typically use an assembly of circular disks or spherical particles to represent the microstructure with bonds acting as the cement between the particles [20, 28–30]. In other cases, sets of discontinuities are explicitly embedded into the rock matrix [31]. Various different ways to model pore collapse also have been proposed and among them, Wang *et al.* [29] used grain shrinkage to simulate intra-granular cracking and grain crushing processes. In these models, porosity is derived based on the spaces generated from the random assembly of the circular disks or spherical particles.

Various deformation mechanisms govern the microstructural changes in rocks. They include crystal plasticity, microcracking, pore collapse, and diffusional mass transfer. In this paper, we focus on two dominant pore-scale mechanisms resulting from purely mechanical, isothermal loading: crystal plasticity and microfracturing. These deformation mechanisms are interdependent on each other, with crystal plasticity triggering microfracturing and microfracturing triggering more crystal plasticity. However, they are herein studied independently in order to determine their overall effect on the macroscopic behavior of porous rocks. This study is particularly useful for understanding the behavior of high-porosity rocks, such as limestone, diatomite, and chalk, where the amount of pore space present per unit volume is quite substantial.

The FEM is used to model pore-scale deformation, with voids embedded explicitly into a crystalline solid matrix to allow investigation of the evolution of deformation and stresses in the solid. Rate-independent crystal plasticity theory is employed, along with a robust ultimate algorithm for tracking the sequence of slip activation in the crystal [32, 33]. Microfracturing is modeled through the strong discontinuity approach, where distinct slips are embedded locally within the elements. This approach is particularly appealing because slips due to microcracking can be represented in the solution without generating additional unknown global degrees of freedom [34–42].

The following notations and symbols are used throughout this work: boldface letters denote tensors and matrices, and subscripted letters denote their scalar components. The summation convention is enforced in this paper. We follow the standard engineering mechanics convention in which compression takes on a negative sign.

2. CRYSTAL PLASTICITY

Common rocks such as granite, marble, quartzite, calcite, and halite are made up of crystals as their basic building blocks. It is generally recognized that crystal deformation is responsible for some brittle microfailure processes in these materials, including the loss of cohesion along grain boundaries and across individual crystals, a process called cataclasis [43]. Crystal deformation may also be responsible for other mechanical processes such as creep and pressure solution, albeit the actual mechanism for the latter process is not so well understood. In brittle crystals, such as quartz crystals, dislocation generation and movement are only possible under atmospheric pressure at temperatures above 820°K [44], but plastic flow is possible at lower temperatures if superimposed hydrostatic pressure prevents fracture [45]. In calcites, twinning occurs predominantly at low temperatures [46]. Deformation twins are also observed at room temperature in hydrostatically compacted limestone samples and may become more pervasive under nonhydrostatic loading and higher stresses [27].

Crystal plasticity is used to model irreversible deformation in the mineral grains, which typically occurs near the periphery of the pores as they change shape to accommodate the increased effective

stress in the solid matrix. An example of crystal plastic deformation is twinning that is observed in calcite grains of limestone specimens near the pore peripheries [48]. Whereas the overall effective stress may be macroscopically hydrostatic, at the pore-scale level, the solid matrix stresses could be far from being hydrostatic. This is due to irregular shape of the pores and their non-uniform size and distribution within the solid matrix.

Crystal deformation differs from continuum deformation in that dislocation generally occurs along glide planes where the atom arrangement is densest (see [49] for other factors affecting dislocation). There is a finite number of glide planes in a crystal arrangement; the challenge lies in identifying which of these glide planes are active. Because there could be more than one active glide plane for a single crystal at any given time, plastic deformation may be viewed as arising from combined activation (although not simultaneously) of slip systems from the set of potentially active systems. Crystal plasticity deals with multiple active constraints at the grain level representing yield conditions on glide planes. Some of these constraints are linearly independent, whereas others are redundant. The constraints are represented by multiple yield surfaces intersecting in a non-smooth fashion [50].

Bishop and Hill [51, 52] were among the first investigators to model the plastic behavior of polycrystalline materials, but their technique did not address the sequence of slip system activation. Budiansky and Wu [53] and Hutchinson [54] employed a trial and error procedure to identify the active slip systems in face-centered cubic (f.c.c.) crystals. Several other algorithms for rate-independent crystal plasticity have been proposed in the literature [55–57], but identifying the linearly independent constraints continues to be a major challenge.

Rate-dependent regularization has been employed by most authors to avoid having to deal with linearly dependent slip systems [58–60]. In rate-dependent formulation, all systems can activate, and slips can be determined according to the viscosity of the material [61, 62]. However, the resolved shear stress becomes a bounded function when the rate sensitivity becomes small, making the set of constitutive equations exceedingly stiff and very difficult to solve [63, 64]. For this reason, it may be more expedient to consider an algorithm that is truly dedicated to rate-independent crystal plasticity.

Borja and Wren [32] presented an algorithm for identifying the independent active constraints in crystals slipping on glide planes, which Borja and Rahmani [33] subsequently implemented into a finite element code. Their algorithm considers the incremental strain in the crystal as being subdivided into substeps, identifying all constraints activated along the way. They used the word ‘ultimate’ for this algorithm to suggest its robust nature in that no potentially active constraint can be missed by the identification procedure. Later, Borja and Rahmani [65] extended the ultimate algorithm for rate-independent crystal plasticity to the finite deformation range. In what follows, we focus on the ultimate algorithm in the infinitesimal range as a means to capture crystal plasticity developing in the solid component of crystalline rocks.

When polycrystalline rocks are subjected to strain, one of the mechanisms of deformation is sliding along the weak crystallographic planes. This mechanism can be manifested either as dislocations or deformation twins [66]. An example of deformation twins in calcite is illustrated schematically in Figure 1. These twins form when the shear stress along the twin plane reaches a certain peak value. Notice a set of twins (in red) with the same orientation developing and intersected by another set of twins (in white) with a different orientation.

The goal of a crystal plasticity algorithm is to identify the activated slip systems and their corresponding slip magnitudes. It is important to distinguish between such plastic deformation and elastic deformation as the former alleviates crystal stress, whereas the latter leads to an increase in crystal stress. As such, plastic slips affect the constitutive relationship, which links the stress in the crystal body to its total deformation. An expression of the constitutive equation can be written using the summation convention as

$$\Delta\sigma_{ij} = c_{ijkl}^e \Delta\epsilon_{kl}^e = c_{ijkl}^e (\Delta\epsilon_{kl} - \Delta\epsilon_{kl}^p), \quad (1)$$

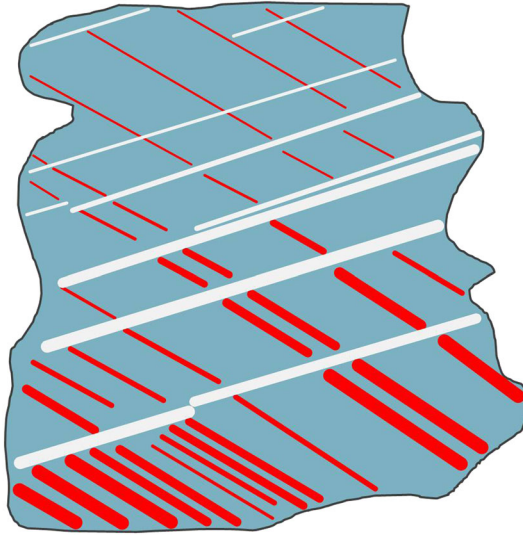


Figure 1. Schematic illustration of calcite twins from the northern Subalpine Chain, France, adapted from Ferrill *et al.* [47]. Two sets of twins with different orientations are shown intersecting each other.

where $\Delta\sigma_{ij}$ is the overall incremental crystal stress tensor, c_{ijkl}^e is the elasticity tensor, which is a function of the elastic moduli, and $\Delta\epsilon_{kl}$ is the incremental strain tensor with elastic component $\Delta\epsilon_{kl}^e$ and plastic component $\Delta\epsilon_{kl}^p$. Elastic strain in crystals is observed as distortion of the lattice structure, which goes away when the stress is removed. Plastic strain, on the other hand, is irreversible and arises from slips on the crystallographic planes.

The plastic strain in a crystal is derived from the contribution of slip from each of the slip systems, which is triggered when the shear stress on the plane exceeds the peak value τ_Y , also known as the yield stress. In crystals, this yield stress can increase when strengthening occurs because of dislocations in the crystal structure. In this work, however, we assume that the yield stress remains constant (perfect plasticity), that is,

$$f^{(\beta)} = |\sigma_{ij}\alpha_{ij}^{(\beta)}| - \tau_Y^{(\beta)} = 0, \quad \beta = 1, 2, \dots, N, \quad (2)$$

where $\tau_Y^{(\beta)}$ is the yield stress at glide plane β . To characterize the slip in system β , we need to know the slip increment $\Delta\gamma^{(\beta)}$, the unit vector $\mathbf{n}^{(\beta)}$ normal to the glide plane, and the slip direction vector $\mathbf{m}^{(\beta)}$, as shown in Figure 2. The plastic component of incremental strain tensor can be obtained from the sum of the slips from all the active systems [50, 67], that is,

$$\Delta\epsilon_{kl}^p = \sum_{\beta_{\text{act}}} \Delta\gamma^{(\beta)} \frac{1}{2} (m_k^{(\beta)} n_l^{(\beta)} + m_l^{(\beta)} n_k^{(\beta)}) = \sum_{\beta_{\text{act}}} \Delta\gamma^{(\beta)} \alpha_{kl}^{(\beta)}. \quad (3)$$

Plastic strain is volume-preserving because slip directions are orthogonal to the glide plane normals. This can be observed from (3) by noting that $\Delta\epsilon_{kk}^p = 0$ because $m_k^{(\beta)} n_k^{(\beta)} = 0$. However, a rock mass can still change in volume as a result of the elastic deformation of the lattice and, more importantly, the expansion or contraction of the pore spaces surrounding a crystal grain.

One major issue in the implementation of crystal plasticity theory lies in the linear dependence of the glide planes, which results in a non-unique combination of active constraints. As an illustration, consider an f.c.c. crystal that has eight octahedral planes shown in Figure 3. Each of these planes has three slip directions, giving rise to 24 potentially active slip systems. However, the incremental plastic strain tensor $\Delta\epsilon_{kl}^p$ is symmetric with only six independent components. Furthermore, the

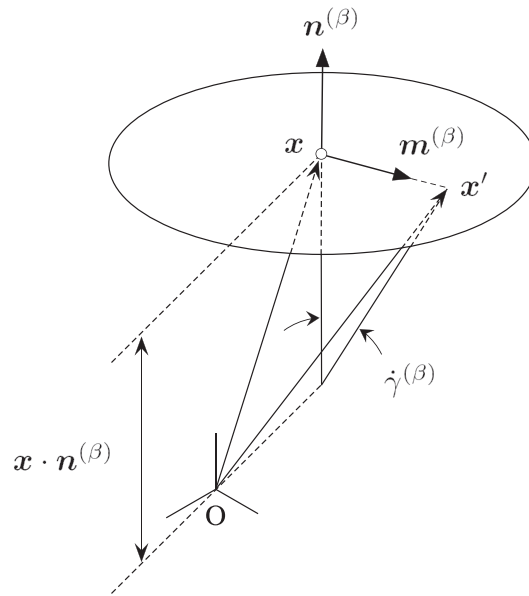


Figure 2. Glide plane β with unit normal $\mathbf{n}^{(\beta)}$ and slip direction $\mathbf{m}^{(\beta)}$.

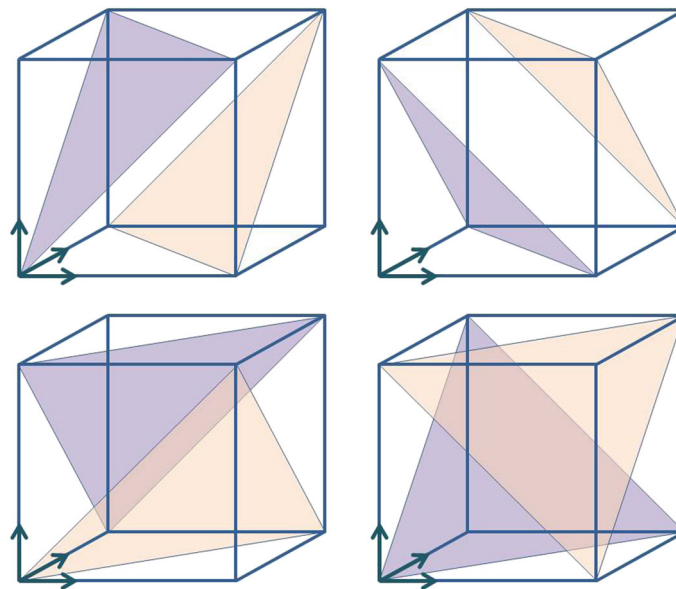


Figure 3. Eight octahedral planes in a face-centered cubic crystal.

constraint that plastic strain is volume-preserving restricts the number of independent components to five. This implies that a given plastic strain tensor can be obtained from many possible combinations of active slip systems. This is addressed in the computation using the ultimate algorithm mentioned earlier.

The basic premise of the ultimate algorithm is to determine the plastic strain increment $\Delta\epsilon_{kl}^p$ as a function of the total strain increment $\Delta\epsilon_{kl}$ in such a way that activated slip systems are identified sequentially. To illustrate the algorithm, consider an initial condition in which the shear stress at each glide plane is less than the yield stress so that the initial response is elastic. The incremental strain $\Delta\epsilon_{kl}$ is then increased linearly until the first slip β_1 (primary system) activates.

The point when this occurs is denoted by $\kappa^{(\beta_1)} \Delta \epsilon_{kl}$. This causes the response to transition from elastic to elastoplastic, with the elastoplastic response reflecting plastic slip produced by the primary system. The remaining portion of the incremental strain is then applied, while the primary system remains active, until a secondary system β_2 activates at $\kappa^{(\beta_2)} \Delta \epsilon_{kl}$. This causes the response to transition from having one slip system to having two active slip systems and so on. For each slip system not belonging to be previous m active slip systems, the ray $\kappa^{(\beta)}$ can be evaluated and used to construct the set

$$\Psi_{m+1} = \left\{ \kappa^{(\beta)} \in R_+ \mid \psi^{(\beta)} \sigma_{ij} \alpha_{ij}^{(\beta)} - \tau_{Y,n} = 0 \right\}. \quad (4)$$

If any of the $\kappa^{(\beta)}$ is less than 1, it implies that the next active slip system β_{m+1} is what produces the smallest element in Ψ_{m+1} . In the event that linearly dependent slip systems are encountered, the redundant systems are discarded arbitrarily. Thus, for a set of slip systems \mathcal{J}_{act} , where $\mathcal{J}_{\text{act}} = \{\beta \in \{1, 2, \dots, N\} \mid f^{(\beta)} = 0 \text{ and } \Delta \gamma^{(\beta)} \geq 0\}$, we can obtain the set of linearly dependent active constraint $\overline{\mathcal{J}}_{\text{act}} \subset \mathcal{J}_{\text{act}}$. It must be noted that while redundant slip systems may be eliminated arbitrarily, the overall crystal stress calculated from this procedure is always unique and does not depend on the specific combination of linearly independent active systems selected.

The input parameters used in the crystal plasticity algorithm describes the mechanical properties of the crystal and its geometry. The material parameters include Young's modulus of elasticity E and Poisson's ratio ν , as well as the initial yield strength τ_Y , which is assumed to be the same for all slip systems. The geometry of the crystallographic planes is described by the normal vector $\mathbf{n}^{(\beta)}$ and slip direction $\mathbf{m}^{(\beta)}$, as well as the Euler angles θ and ϕ , which describe how the crystal reference frame is oriented with respect to the fixed reference frame. As shown in Figure 4, the crystal coordinates are obtained by a positive (right-hand rule) rotation of θ about the y -axis followed by a positive rotation of ϕ about the z_c -axis. The third Euler angle is zero.

The crystal plasticity algorithm consists of a predictor phase (Box 1) and a corrector phase (Box 2). The flow charts are more elaborate than the conventional plasticity algorithm because of the multi-surface nature of the yield condition and the filtering of the yield constraints to remove the linearly dependent constraints. The algorithm must also accommodate for slip systems that deactivate during substepping (Step 3 of Box 2). As noted in [32, 33], the algorithm is unconditionally convergent as well as exact for loading imposed as a ramp function.

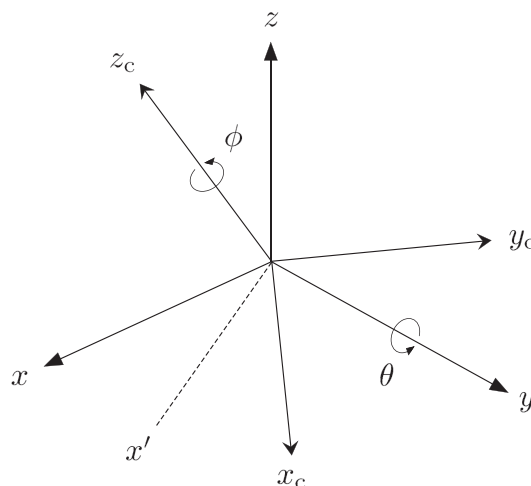


Figure 4. Euler angles describing the relationship between the crystal reference frame and the fixed reference frame. The crystal coordinates are obtained by a positive (right-hand rule) rotation of θ about the y -axis followed by a positive rotation of ϕ about the z_c -axis.

Box 1. Predictor phase for crystal plasticity algorithm

- Step 1. Compute the trial stress $\sigma_{ij,n+1}^{tr} = \sigma_{ij,n} + c_{ijkl}^e \Delta \epsilon_{kl}$.
 Assemble \mathcal{J}^{tr} , the set of active slip systems based on the trial stress,
 $\mathcal{J}^{tr} = \{\beta \mid \psi^{(\beta)} \sigma_{ij,n+1}^{tr} \alpha_{ij}^{(\beta)} - \tau_{Y,n} > 0\}$.
- Step 2. Check: Is \mathcal{J}^{tr} a null set?
 Yes, response is elastic. Set $\sigma_{ij,n+1} = \sigma_{ij,n+1}^{tr}$ and $c_{ijkl} = c_{ijkl}^e$.
 Exit predictor phase.
- Step 3. No, response is plastic.
 Assemble \mathcal{J}_{act} , the set of active slip systems in the current time step,
 $\mathcal{J}_{act} = \{\beta \mid \psi^{(\beta)} \sigma_{ij,n} \alpha_{ij}^{(\beta)} - \tau_{Y,n} > 0\}$.
 Call Box 2.
- Step 4. Update crystal stress and tangent operator for the next time step
 $\sigma_{ij,n+1} = \sigma_{ij,n}$, $c_{ijkl} = c_{ijkl}^{ep}$.

Box 2. Corrector phase for crystal plasticity algorithm

- Step 1. If \mathcal{J}_{act} is a null set, go to Step 5.
- Step 2. Identify linearly independent slip systems in \mathcal{J}_{act} and store in $\overline{\mathcal{J}}_{act}$.
- Step 3. Compute $\Delta \gamma^{(\beta)}$ for each element in $\overline{\mathcal{J}}_{act}$.
 Drop the inactive slip systems, indicated by negative $\Delta \gamma^{(\beta)}$.
- Step 4. Compute $c_{ijkl} = c_{ijkl}^{ep}$ for the current $\overline{\mathcal{J}}_{act}$.
- Step 5. Compute $\kappa^{(\beta)}$ for all slip systems not in $\overline{\mathcal{J}}_{act}$. Assemble Ψ_{m+1} .
- Step 6. Is any $\kappa^{(\beta)} < 1$?
 Yes, response is plastic. Update:
 $\sigma_{ij,n} \leftarrow \sigma_{ij,n} + \kappa^{(\beta_{m+1})} c_{ijkl}^{ep} \Delta \epsilon_{kl}$
 $\Delta \epsilon_{ij} \leftarrow \Delta \epsilon_{ij} - \kappa^{(\beta_{m+1})} \Delta \epsilon_{ij}$.
 Include β_{m+1} into the set $\overline{\mathcal{J}}_{act}$.
 No, response is elastic.
- Step 7. If $\kappa^{(\beta_{m+1})} < 1$, go to Step 2.
- Step 8. Return to Box 1.

3. MICROFRACTURING

Microfracturing involves the formation of fine cracks in the pore scale. A large increase in the strain results when slip occurs on the crack that is confined to a very small region. Oftentimes, this coincides with bifurcation of material response characterized by the loss of uniqueness of the deformation mode [68]. Microfractures have been observed to form in close proximity to imperfections in porous rocks. Micritic limestone with an initial porosity of 13.4% undergoing hydrostatic compaction was shown to develop a halo of cataclastic damage surrounding the macropore [26]. This halo consists of tiny cracks that form and intersect one another all around the perimeter of the pore. Microcracks also have been observed to develop in triaxially deformed specimens of limestone, propagating from the pores and coalescing to reach lengths much larger than the pore diameter. Hirth and Tullis [24] observed axial microcracks forming at the top and bottom of quartzite pores under triaxial compression, which became more closely spaced as the differential stress increased.

In this paper, we simulate the process of microfracturing using the strong discontinuity approach. ‘Strong discontinuity’ refers to a jump in the displacement field over an idealized surface with zero thickness. This is in contrast to ‘weak discontinuity’ where a kink on the displacement field occurs, resulting in a jump in the strain field. We emphasize that the microfractures addressed in this work pertain to random, discontinuous cracks as motivated by the experimental observations described in

the first paragraph of this section and not to a continuous crack that requires a special tracking algorithm to delineate its geometry of propagation [69, 70]. We also emphasize the importance of a full three-dimensional analysis to accommodate the kinematics of three-dimensional randomly forming and discontinuous cracks. The development of the strong discontinuity approach for simulating localized deformation has gained momentum since the mid-1990s because of the shortcoming of classical plasticity theory to provide a characteristic length scale needed for predicting the response beyond the bifurcation point [71, 72].

We employ the assumed enhanced strain (AES) FEM to improve the performance of the finite elements in resolving the kinematics of strong discontinuity. The AES method introduces an additional slip degree of freedom within a localizing element. An advantage of the AES approach is that the enhancement is carried out on the element level without changing the size of the global system of equations to solve. Furthermore, it can accommodate random and disconnected cracks and can smear strain concentrations around the crack tip much better than the extended FEM, which requires additional crack tip enhancements to avoid locking around the crack tips [73, 74]. The present work features an enhancement of hexahedral finite elements to accommodate the kinematics of microfracturing at the pore scale. We note a clear separation of scales in the present work in that the AES approach is not used to propagate the microfractures to the next larger scale, but rather, to simply capture the micromechanics of the underlying overall constitutive law. In other words, the microfractures are not traced, unlike in all previous works, but instead are simply allowed to emerge in highly stressed elements.

To illustrate the capture of microfracturing with the AES approach, we consider a domain \mathcal{B} in a two-dimensional setting shown in Figure 5. We can view randomly oriented microfractures as reflecting the slip orientations of the most highly stressed crystals, typically located near the peripheries of the pores. In the present approach, each damaged element could contain no more than one microfracture. The physical microfracture may lie exclusively within the element interior and not necessarily intersect the element sides, but the smearing process characteristic of the AES approach assumes the crack to extend all the way to the element sides, such as the microfracture that partitions a finite element into sides A and B in Figure 5. This results in the development of displacement jumps not only on the surface of the microfracture but also on the sides of the neighboring elements intersected by the microfracture. The kinematics of the microfracture is strictly local to the damaged element, and the slip degree of freedom is eliminated prior to global assembly by the traditional technique of static condensation [75]. The bulk material outside the microfracture is assumed to undergo elastic unloading, although it is also possible to consider bulk plasticity outside the discontinuity zone [76, 77].

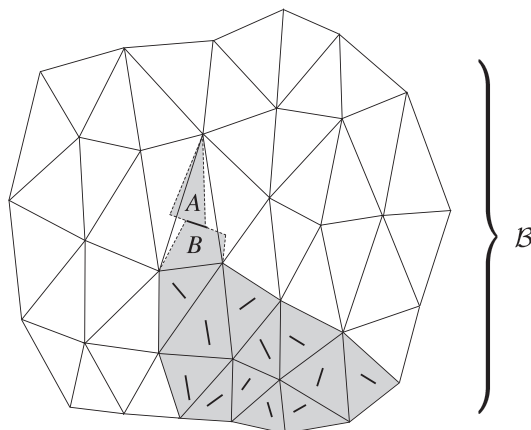


Figure 5. Randomly oriented and disconnected microfractures: each shaded finite element contains no more than one microfracture. Assumed enhanced strain approach extends the microfracture all the way to the sides of the element, partitioning the element domain into sides A and B .

Two questions naturally arise with the proposed approach: (i) what triggers microfracturing, and (ii) how does a microfracture evolve after it has been triggered? In quartz crystals, the stress required for the tensile fracture depends on the geometry of the initiating imperfection. Sharp notches, for example, require a surface energy of approximately 2 J/m² to fracture at room temperature [78]. Furthermore, quartz shows a propensity to fracture along rhombohedral planes, with the presence of water reducing the stress required to fracture. Common sedimentary rocks, however, contain not only quartz but also calcite, dolomite, gypsum, and all the clays. In calcite, many preexisting defects can initiate a crack, including closed pores, clay mineral precipitates, and steps. Micrographs [79] indicate that the fracture surface in calcite intersects many such defects so that the conventional Griffith criterion cannot be used because all defects are relevant. Taking all these factors into consideration would result in considerable uncertainties in the formulation. Thus, our microfracturing criterion revolves around the simplified crystal structure described previously, with the simple rule that microfracturing initiates on any possible slip plane in the crystal that is most stressed.

Once the most stressed (primary) slip system is detected, the normal \mathbf{n} and slip direction \mathbf{m} of the microfracture are defined. In the case of an interface contact, the stress in the element can be calculated as

$$\sigma_{ij}^e = c_{ijkl}^e : \frac{1}{V} \int_{\Omega_e} [\epsilon_{c,kl} - \zeta_t^e (f_k^h \otimes m_l)^s] d\Omega, \tag{5}$$

where $\epsilon_{c,kl}$ is the conforming strain field, ζ_t^e is the tangential slip within an element, and f^h is an arbitrary smooth blending function. The blending function is used to recover the concentrated displacement jump from the conforming displacement field (see Chapter 7 of [50] for details on this blending function). In the finite element implementation, an eight-point Gauss integration rule is employed to calculate the volume integral. A constant slip interpolation is used, which implies that the tangential slip ζ_t^e is constant for each enhanced element.

Knowledge of the position of the microfracture within an enhanced hexahedral element is required to define the blending function f^h . Normal separation \mathbf{n} and slip direction \mathbf{m} are insufficient to identify the position of the microfracture. This is illustrated in Figure 6 where three

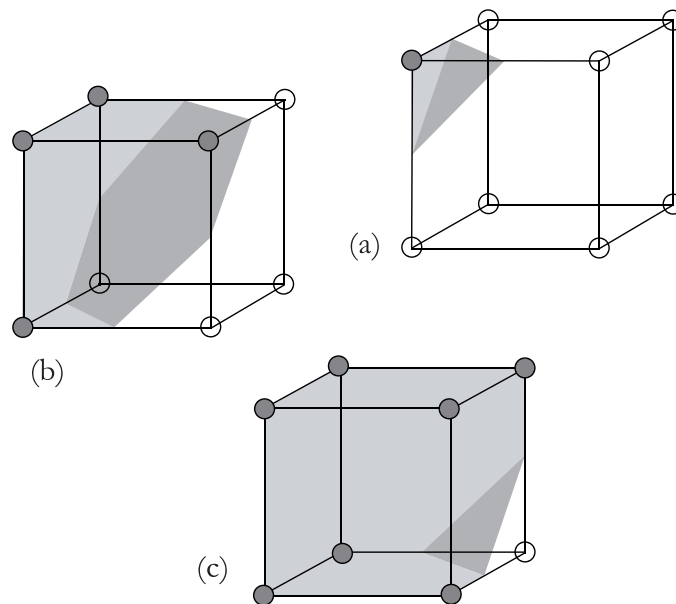


Figure 6. Enhancement of hexahedral finite elements to accommodate a microfracture: darker planes denote planes of microfracture; filled nodes lie on the ‘positive’ side of the microfracture; empty nodes lie on the ‘negative’ side.

possible configurations of a microfracture with identical \mathbf{n} and \mathbf{m} are shown. The position of the microfracture is assigned arbitrarily to an element because microfractures are discontinuous across element boundaries, and thus, the microfracture edge of one element does not need to be aligned with that of its neighboring element. In the present simulations, every element assumes configuration (b) in Figure 6, where both the ‘positive’ and ‘negative’ sides of the microfracture contain four nodes of the enhanced hexahedral element.

Discontinuous deformation can be used to capture microfracturing of the mineral grains. Whereas the balance of linear momentum and the bulk constitutive law must be satisfied within a conventional finite element interpolating a conforming displacement field, finite elements containing a microfracture are also required to satisfy an interface constitutive law on the plane of discontinuity. For a porous rock, this interface constitutive law is the cohesive frictional law in which the occurrence of slip is signified by the resolved shear stress exceeding the combined frictional and cohesive resistance on the most highly stressed slip system.

The interface constitutive law must account for slip weakening, a process in which the strength of an intact rock drops to a purely frictional value on the surface of discontinuity. The process involves combined friction hardening–cohesion softening [50, 80]. The frictional resistance is assumed to increase linearly from zero at the point of localization to the full value over a characteristic sliding distance ζ^+ , while the cohesion drops linearly to zero over the same characteristic sliding distance. The slip weakening constitutive law can be written in terms of an interface yield function

$$f_t^e = \begin{cases} |\tau^e| + \mu^e \sigma^e \zeta_t^e / \zeta^+ - c^e (1 - \zeta_t^e / \zeta^+) = 0, & \text{if } 0 \leq |\zeta_t^e| \leq \zeta^+, \\ |\tau^e| + \mu^e \sigma^e = 0, & \text{if } |\zeta_t^e| > \zeta^+, \end{cases} \quad (6)$$

where the superscript ‘e’ pertains to the localizing element, ζ_t^e is the tangential slip on the discontinuity, μ^e is the coefficient of friction on the interface, σ^e is the stress normal to the surface of discontinuity (negative under compression), and c^e is the cohesion within the localizing element. The initial value of cohesion is equal to the shear stress at the point of localization so that the yield function is equal to zero when slip initiates.

In the event that the interface separates, the normal stress must necessarily drop to zero, and thus, the frictional resistance must also drop to zero. This process is represented in Equation (6) by the vanishing of the second (frictional) term. As a result, the shear stress on the plane goes to zero once the cohesion disappears over the characteristic sliding distance. In addition, the fractured element must also satisfy the conditions that the second tangential stress component as well as the stress component normal to the plane are zero. This is expressed in the form of the yield conditions f_{t2}^e and f_n^e as follows:

$$f_{t2}^e = \begin{cases} |\tau_2^e| - c_2^e (1 - \zeta_{t2}^e / \zeta_{t2}^+) = 0, & \text{if } 0 \leq |\zeta_{t2}^e| \leq \zeta_{t2}^+, \\ |\tau_2^e| = 0, & \text{if } |\zeta_{t2}^e| > \zeta_{t2}^+, \end{cases} \quad (7)$$

$$f_n^e = \sigma^e = 0. \quad (8)$$

Therefore, for any finite element containing a microfracture, we can quantify three types of discontinuity: two tangential slips (ζ_t^e and ζ_{t2}^e) and normal separation (ζ_n^e). Furthermore, the stress in the element as depicted in Equation (5) must also take into account the two additional discontinuities.

Box 3 shows a summary of the finite element implementation of the AES approach. The first step checks for the localization condition in the crystals. Once the primary slip system is identified within an element, the slip normal and slip direction for the crystal are used by the algorithm to determine the geometry of the microfracture and calculate the amount of microslip on the active plane of the crystal. By using the same crystal configuration for capturing both ductile deformation

due to crystal slips and brittle deformation due to microfracturing, we can make a more meaningful comparison of the two micromechanisms of deformation.

Box 3. Finite element implementation of the AES approach

- Step 1. Check: has the material localized?
 No, elastic deformation continues.
 Yes, fracture is initiated. Set
 \mathbf{n}^e = slip normal of the primary slip system
 \mathbf{m}^e = slip orientation of the primary slip system.
- Step 2. For every localized element,
 a. Calculate:
 - Plastic strain as a function of \mathbf{n}^e and \mathbf{m}^e ;
 - Balance of linear momentum and interface yield conditions as a function of displacement and slip unknowns.
 b. Linearize the equations.
 Obtain element stiffness and residual matrices.
 c. Statically condense slip degrees of freedom.
 Obtain new element stiffness and residual matrices.
- Step 3. Solve the global system of equations. Obtain displacement dofs.
 Step 4. Obtain slip rate increments for each localized element.
 Step 5. Repeat Steps 1–5 until convergence is achieved.
 Step 6. Store converged displacement and slip dofs.

4. SIMULATION RESULTS

We now investigate the pore-scale mechanical responses of a crystalline material with properties similar to those of limestone. It is generally recognized that even at room temperature and pressure, both crystal plasticity and microfracturing can dominate the micromechanisms of deformation in limestone. Laboratory experiments involving mechanical deformation of limestone have been conducted, and instances of crystal plasticity and microfracturing are well documented through observations at the pore scale using either optical micrograph in plain transmission light or backscattered scanning electron microscope [27, 48]. Table I shows the mechanical properties used in the simulations. The crystal yield stress is assumed to be constant for all slip systems and is denoted by the symbol τ_Y .

The solid matrix microstructure is modeled using the FEM. A cube is used to represent a representative elementary volume (REV), which, by definition, is larger than the pore scale but smaller than the specimen scale. We consider two different types of inhomogeneities in the REV, namely, the void distribution and crystal orientation. The voids are modeled explicitly as hollow inclusions with cubical geometry. This allows us to look more closely into the stress–strain behavior and patterns surrounding the voids. Even though voids in reality have more complex geometry than the idealized shape assumed, this simple geometry is capable of capturing not only smooth boundaries but also sharp edges, which may introduce local stress concentration. The model contains four randomly positioned voids with varying sizes, as shown in Figure 7(a), resulting in an overall porosity of 3.8%. The different sizes of the voids allow us to investigate the effect of pore size on fracture and

Table I. Material properties for limestone-like rock.

Parameter	Symbol	Value
Young's modulus	E	20,000 MPa
Poisson's ratio	ν	0.30
Crystal yield stress	τ_Y	30 MPa

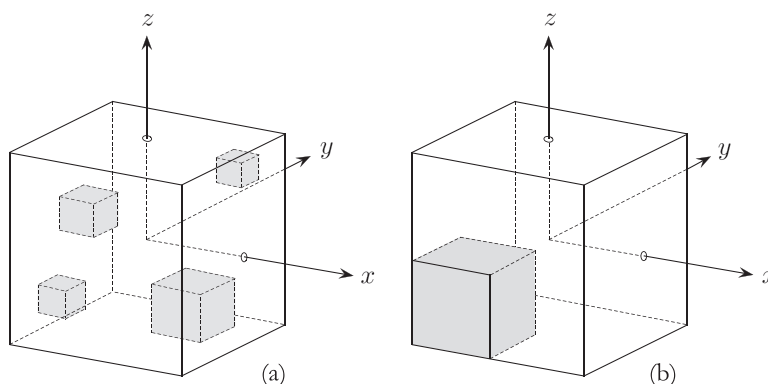


Figure 7. Partition of the representative elementary volume into (a) solid material (white region) and air void (gray region) and (b) two crystal groups with Orientation #1 (white region) and Orientation #2 (gray region).

Table II. Euler angles of the crystal groups in degrees.

Orientation	θ	ϕ
#1	0.0	22.0
#2	0.0	0.0

crystal plasticity initiation. Note that the REV represents a specific pore-scale structure and does not necessarily suggest a recurring microstructure in nature.

Limestone has a complex crystal lattice, being primarily made up of calcite, dolomite, and aragonite. Both calcite and dolomite have rhombohedral crystal structures, while aragonite has a rhombic structure [81]. This gives rise to many forms and lattice directions. Because of this complexity, we make a simplifying assumption in our model that the crystal lattice is made up of f.c.c. crystals. Despite this simplification, we believe that the simulation will still shed light onto the important micromechanisms of deformation in a polycrystalline rock containing voids and other forms of heterogeneity.

An f.c.c. crystal has eight $\{1\ 1\ 1\}$ octahedral planes. Each of these planes has three $\langle 110 \rangle$ slip directions, resulting in 24 potentially active slip systems. However, only 12 slip systems can activate at any given time because the eight octahedral planes form conjugate pairs where an active plane in a pair implies that the other plane in the same pair is inactive. The REV contains two crystal groups with different crystal orientations. Figure 7(b) illustrates the configurations of the two crystal groups, whereas Table II summarizes the values of the Euler angles for these two groups.

The REV is a $20 \times 20 \times 20 \mu\text{m}^3$ volume partitioned into $18 \times 18 \times 18$ cubical elements. In both the crystal plasticity and microfracturing simulations, each solid element deforms elastically at the beginning of the simulation until the yield condition for one of the slip systems is reached, indicating crystallographic slip. In crystal plasticity, slips on the crystallographic planes continue as long as the slip system remains active. However, in the microfracturing simulations, slip on the primary system indicates localization triggering strong discontinuity. Slip weakening then governs the constitutive behavior on the surface of discontinuity, causing the transition from a cohesive frictional behavior to a purely frictional behavior (or frictionless behavior in the case of a normal separation). In all the simulations carried out, the load imposed on the boundary is always driven by a prescribed boundary deformation.

A homogenization procedure is needed to obtain the average behavior at the scale of the REV [82]. There are many different ways to homogenize the stress responses. For a finite element mesh with uniformly sized cubical finite elements, the stresses can be homogenized simply by calculating the volume-averaged responses at the integration points, that is,

$$\sigma_{ij} = \frac{1}{V} \int_V \sigma_{ij}^e dV = \frac{1}{n_{\text{int}}} \sum_{n=1}^{n_{\text{int}}} (\sigma_{ij})_n, \quad (9)$$

where σ_{ij} is the overall Cauchy stress tensor, σ_{ij}^e is the stress tensor at each element, $(\sigma_{ij})_n$ is the stress tensor at each integration point, and n_{int} is the total number of integration points in the REV, including the phantom integration points for the void spaces (because the voids are part of the total volume). Different invariants of the overall stress, such as the mean normal stress and the von Mises stress, can be calculated readily from the volume-averaged stress tensor.

We consider two different loading conditions, namely, combined shear and extension, and combined compression-lateral extension loading. Both crystal plasticity and microfracturing simulations are conducted for each loading condition. We also consider different crystal orientations to better understand the effect of this parameter on the ensuing micromechanical responses. All integration points are assumed to be initially stress-free.

4.1. Combined shearing and extension

In this simulation, the REV undergoes affine transformation on its six faces, producing shearing and expansion in the volume. The displacements on the boundaries are incremented linearly at each time step. The incremental displacements (in nm) applied on the faces of the REV take the form

$$\begin{Bmatrix} \Delta u_x \\ \Delta u_y \\ \Delta u_z \end{Bmatrix} = 0.03 \begin{Bmatrix} (x + 10) + (z + 10) \\ 0 \\ (x + 10) + (z + 10) \end{Bmatrix} \text{ nm}, \tag{10}$$

where x, y, z are Cartesian coordinates in microns. Note that the displacement in the y -direction is restrained, creating a plane strain condition on the xz -plane (Figure 8(a)). This deformation field preserves the planar configuration of all six faces of the volume, even though the deformation field in the interior of the volume remains irregular because of microstructural effects. For the microfracturing simulation, the characteristic sliding distance ζ^+ is assumed to be very small such that slip weakening occurs in one time step.

Figure 9(a) shows cutouts of the REV revealing the inelastic deformation developing in the interior of the volume due to crystal plasticity. A yield zone emanates from a corner of the larger void and merges with another yield zone emanating from a nearby smaller void. We recall from Equation (3) that the continuum incremental plastic strain for a crystal is the sum of the contributions from the activated slip systems. The plastic strain contour plotted in Figure 9 is the cumulative plastic strain

$$\varepsilon^p = \sum_{n=1}^{n_{\text{step}}} \sqrt{\Delta \epsilon_{kl}^p \Delta \epsilon_{kl}^p}, \tag{11}$$

where n_{step} is the number of load increments over which the plastic strain is accumulated.

By comparison, Figure 9(b) and (c) portray the cumulative tangential slip and normal separation, respectively, generated by the AES approach for the same imposed boundary deformation

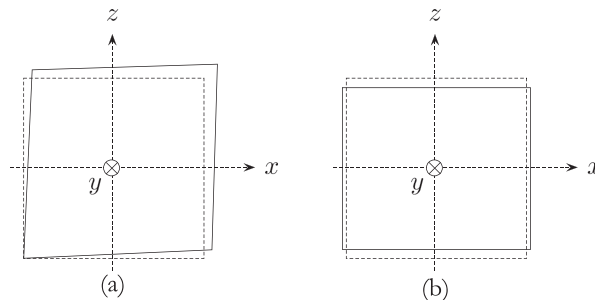


Figure 8. Affine deformation of six faces of the representative elementary volume: (a) combined shearing and extension; and (b) vertical compression-lateral extension with net volumetric compression.

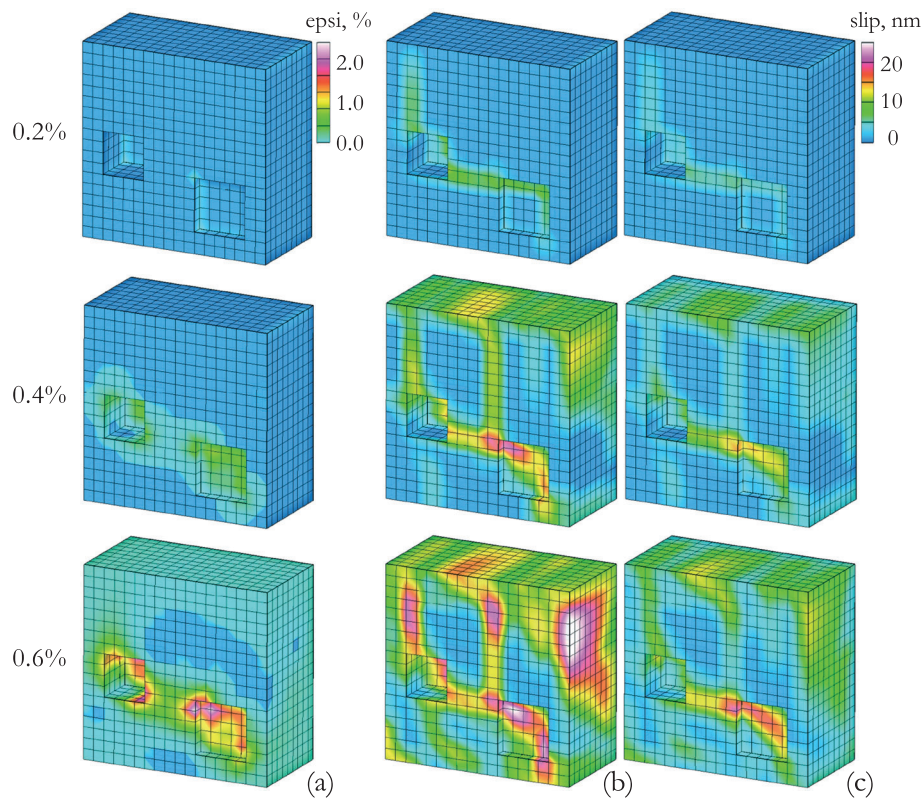


Figure 9. Evolution of yield and damage zones from combined shearing–extension: (a) yield zone induced by crystal plasticity; (b) tangential slip zone induced by microfracturing; and (c) normal separation induced by microfracturing. Numbers in percent are imposed volumetric strain on the representative elementary volume. Color bars: epsi , ε^p ; slip, tangential slip and normal separation (same color bar).

(for conciseness, we have omitted the plots for the second tangential slip that has a similar pattern as compared with the plotted tangential component). We remark that the tangential slip and normal separation have the units of length, whereas the plastic strain is a dimensionless quantity, and so the color bars for the slip/separation contours may not be compared directly with that for the strain. Nevertheless, the contours for the microslip and microseparation show more pervasive damage to the volume compared with the more limited yield zone generated by the crystal plasticity simulation for the same imposed boundary deformation. We observe that the microslips also originate from the voids and coalesce to form an irregularly shaped damage zone. The latter zone, which may be inferred to trigger fracturing on the mesoscopic to macroscopic scale, is seen to develop largely from the coalescence of the microfractures. The geometry of this damage zone is influenced to a great extent by the spatial distribution of the voids.

The largest magnitude of crystal plastic slip appears to occur at the corners of the voids, and this is most likely due to the fact that they are sites with the greatest stress differential, causing high shear stresses to develop on the slip planes that induce crystallographic slips. On the other hand, for the AES simulation, damage is observed to develop along a curved zone passing through two of the largest voids when plasticity has just initiated, splitting the volume apart. High density of microfractures with large slips are expected to develop close to this surface. As the simulation progresses, branches are observed to occur from the curved damage zone to the boundary of the REV.

Figure 10 shows plots of the overall von Mises stress versus overall volumetric strain. The von Mises stress σ is a scalar measure of deviatoric stress that can be obtained from the equation

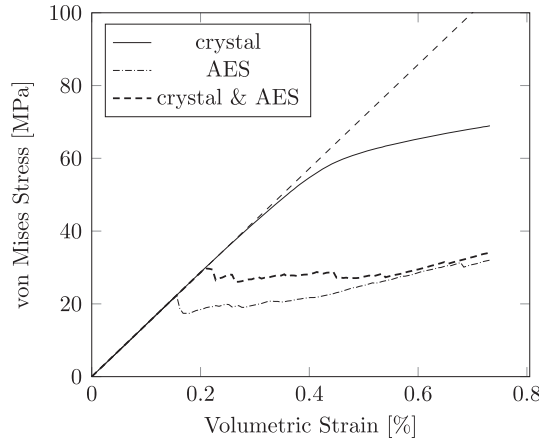


Figure 10. Combined shearing and extension: overall von Mises stress versus overall volumetric strain curves for the representative elementary volume. AES, assumed enhanced strain.

$$\sigma = \sqrt{\frac{(\sigma_1 - \sigma_2)^2 + (\sigma_2 - \sigma_3)^2 + (\sigma_1 - \sigma_3)^2}{2}}, \tag{12}$$

where σ_1 , σ_2 , and σ_3 are the three principal Cauchy stresses. The overall volumetric strain ϵ_{vol} , on the other hand, is obtained by taking the sum of the three principal strains, that is,

$$\epsilon_{vol} = \epsilon_1 + \epsilon_2 + \epsilon_3. \tag{13}$$

In this example, a deviatoric measure of stress (i.e., the von Mises stress) can be paired with a volumetric measure of strain because of the combined shearing–extension deformation imposed on the REV.

Figure 10 suggests that the behavior of the REV is elastic prior to the initiation point, as can be observed from the linear stress–strain response up to a von Mises stress value of around 20 MPa. Once plastic slip initiates, the curve deviates from a straight line. Crystal plasticity produces a more ductile response. The slope of the stress–strain curve decreases as more slip systems activate, thus putting a cap on the value of the von Mises stress, but there is no softening observed. The AES simulation, on the other hand, produces a more brittle response. The simulation generates slip such that the shear stress on the microfracture can only be as high as the frictional resistance generated from the normal compressive stress. However, when a microfracture splits in opening mode, no frictional resistance can develop. Numerous hexahedral elements experience a splitting mode as a result of the imposed volumetric expansion, thus creating intermittent softening response of the REV. Figure 10 also plots the results of simulations combining crystal plasticity and microfracturing. In this simulation, crystal plasticity is allowed to develop up to a certain critical norm of plastic strain, after which microfracturing ensues and assumes the geometry and slip direction of the last activated slip system. In this simulation, the critical norm of plastic strain used is 0.1%, resulting in a stress–strain response that is intermediate between the fully ductile and fully brittle responses.

4.2. Combined compression–lateral extension

For the second loading condition, we carry out simulations resembling a biaxial compression setting. The displacements (in nm) are incremented linearly with each time step according to the relation

$$\begin{Bmatrix} \Delta u_x \\ \Delta u_y \\ \Delta u_z \end{Bmatrix} = \begin{Bmatrix} 0.02x \\ 0.02y \\ -0.10z \end{Bmatrix} \text{ nm}, \tag{14}$$

where x, y, z are in microns. Figure 8(b) portrays the affine boundary deformation showing that the REV is compressed vertically as it expands in the two lateral directions by an amount equal to 20% of the vertical compression.

Figure 11 depicts the development of yield zones for crystal plasticity and damage zones for the AES simulations. Yielding is seen to initiate at the side of the pores and progressing in the lateral direction consistent with the direction of vertical compression. As the simulation continues, other elements eventually experience sufficiently large shear stresses; however, inelastic deformation continues to be largest on the sides of the voids. Because yielding of the primary slip systems is reached

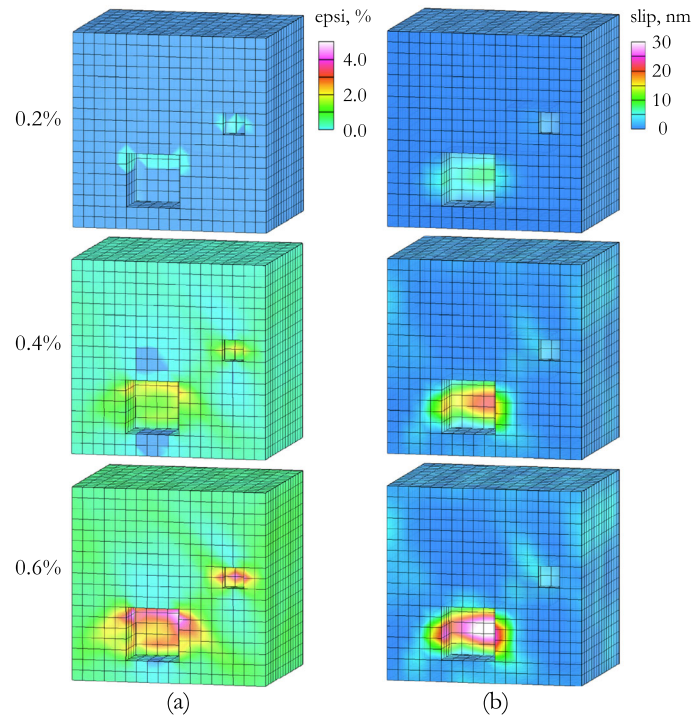


Figure 11. Evolution of yield and damage zones for the combined vertical compression–lateral expansion simulations: (a) yield zone induced by crystal plasticity; and (b) tangential slip zone induced by microfracturing. Numbers in percent are imposed volumetric strain on the representative elementary volume. Color bars: $\text{epsi}, \varepsilon^p$; slip, tangential slip.

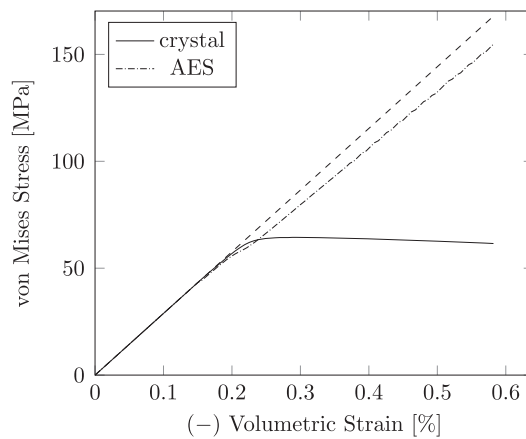


Figure 12. Combined vertical compression–lateral extension: overall von Mises stress versus overall volumetric strain curves for the representative elementary volume. AES, assumed enhanced strain.

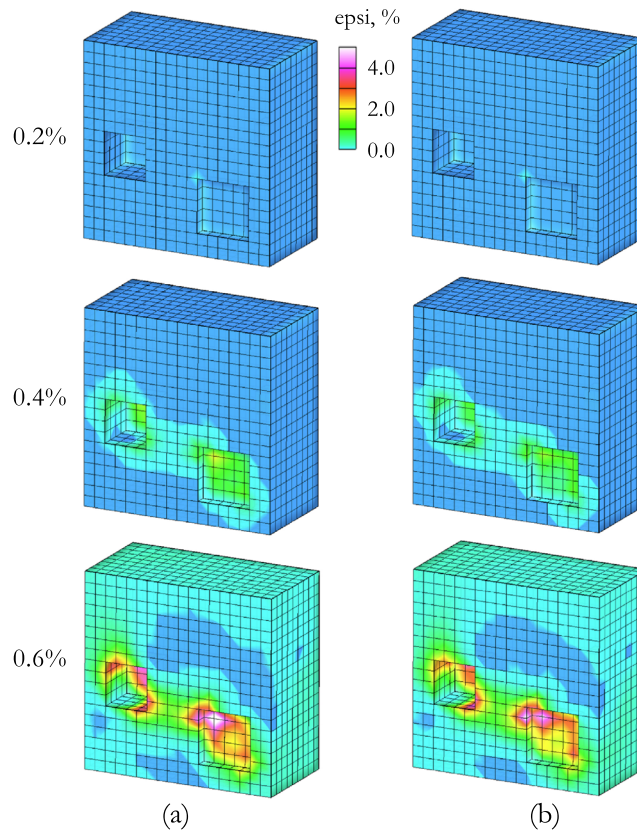


Figure 13. Evolution of crystal yield zone for the combined shearing–extension simulation: (a) homogeneous crystal orientation; and (b) heterogeneous crystal orientation. Numbers in percent are imposed volumetric strain on the representative elementary volume. Color bar: $\epsilon^p, \%$.

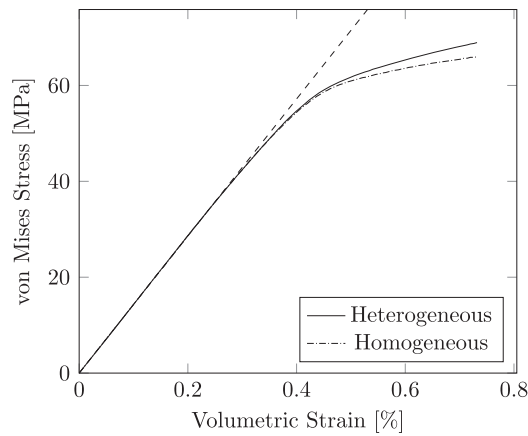


Figure 14. Comparison of the overall von Mises stress versus overall volumetric strain responses for combined shearing–extension simulation for the homogeneous and heterogeneous crystal orientation simulations.

earlier on the sides of the voids, yield and damage zones propagate outward from the voids in the lateral direction in a way as to collapse or squash the pores in the vertical direction. We observe that the extent of the yield zone for crystal plasticity is somewhat more pervasive than the extent of the damage zone for the microfracturing simulations. This is because the applied deformation favors the development of higher compressive stresses, thereby enhancing the frictional resistance

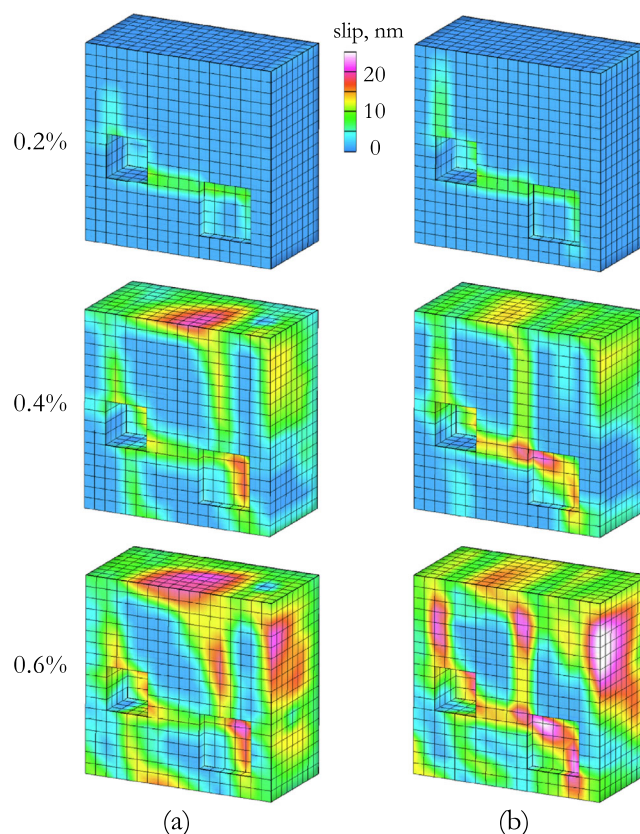


Figure 15. Evolution of tangential microslip for the combined shearing–extension simulation: (a) homogeneous crystal orientation; and (b) heterogeneous crystal orientation. Numbers in percent are imposed volumetric strain on the representative elementary volume.

of the rock. This is a stark contrast to the previous example where the development of microcracks was enhanced by the volume expansion.

Figure 12 compares the overall stress–strain curves for the two micromechanisms of deformation. Plastic slip initiates at a volumetric strain of approximately 0.16%. Beyond this point, the two curves begin to diverge. For crystal plasticity, the yield strength is dictated by the activated slip systems so that as more slip systems activate, the von Mises stress eventually reaches a plateau. However, in the AES simulations, the primary slip system transforms into a frictional interface so that hardening ensues as the normal stress increases. Because the REV experiences a net volume decrease, larger normal stresses develop on the slip surfaces, causing an increase in the frictional resistance of the elements. In most of the elements that localized, the increase in normal stresses has allowed a build-up of shear stresses on the slip surfaces to the point where these interfaces eventually stopped slipping.

4.3. Impact of crystal orientation

It has long been recognized that crystal orientation can impact the overall stress–strain responses of crystalline materials [83]. To look into this aspect further, we repeat the simulations of Section 4.1 by removing the heterogeneity in crystal orientation and comparing the resulting stress–strain responses of the REV with those generated from the simulations with two crystal groups. For purposes of comparison, the term ‘homogeneous’ in the context of this section pertains to a porous crystalline solid with uniform Euler angles of $\theta = \phi = 0^\circ$; the term ‘heterogeneous’ pertains to the REV with the two crystal groups defined in Table II. The pore distributions are identical for the homogeneous and heterogeneous simulations.

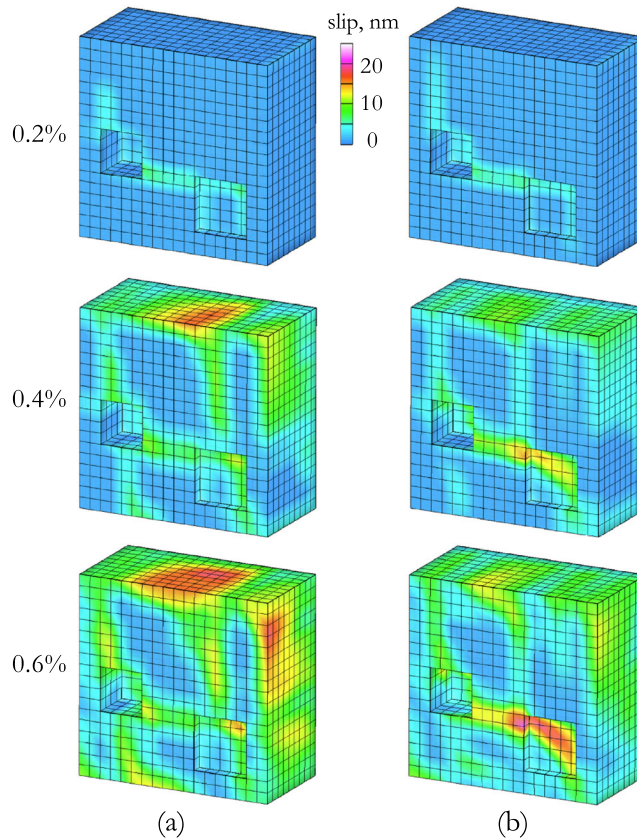


Figure 16. Evolution of normal microseparation for the combined shearing–extension simulation: (a) homogeneous crystal orientation; and (b) heterogeneous crystal orientation. Numbers in percent are imposed volumetric strain on the representative elementary volume.

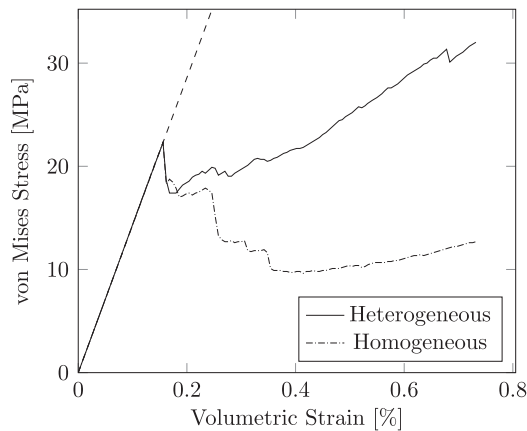


Figure 17. Comparison of the overall von Mises stress versus overall volumetric strain responses for combined compression–lateral extension simulation for the homogeneous and heterogeneous crystal orientation simulations.

Figure 13 compares the plastic yield zones generated by the homogeneous and heterogeneous crystal orientation simulations for the same imposed boundary displacements considered in Section 4.1, that is, combined shearing–extension. The general pattern of yielding is nearly the same, although minor differences can be spotted upon closer examination. These differences translate to the next level into a different stress–strain plot. Figure 14 shows the ductile stress–strain

responses for the two simulations suggesting that the heterogeneous crystal orientation produces a stiffer response. Of course, this is not always true, as noted in [32, 65], inasmuch as the mechanical response of a crystal is known to depend on the direction of loading relative to the crystal orientation. In other words, for the same loading direction, a given crystal orientation could make it either easier or harder for the system to slip.

We repeat the simulations, this time using the AES approach to assess how the heterogeneity in crystal orientation could impact the brittle response of a porous material. Figures 15 and 16 show the evolution of tangential and normal microslip zones, respectively. Although the general pattern of damage remains fairly similar for either case, the level of damage, measured in terms of the magnitude of tangential and normal slips, is substantially different. More specifically, the zones of most intense tangential slip and most intense normal separation are not the same, implying a more noticeable impact of crystal orientation on the brittle mode of deformation at the pore scale. Notice in both the tangential and normal separation contours, for example, that the most intense damage is no longer around the periphery of the larger void when the crystal orientation is assumed to be uniform.

Figure 17 compares the two brittle stress–strain responses, suggesting a softer response for the REV with a uniform crystal orientation. This difference in the responses is not as predictable as the much smoother stress–strain responses resulting from classic crystal plasticity simulations (Figure 14). Because of the ‘noise’ generated by sudden slip weakening when each element is enhanced, the AES approach produces an erratic overall stress–strain response for the REV. It is likely that the higher von Mises stress observed with the heterogeneous crystal orientation simulation is due to obstruction of slip by other grains in the neighborhood of the element that developed a microfracture. However, as noted earlier, the response of a crystal depends on the direction of load relative to the crystal orientation, and so, it is possible that for a different imposed load, an opposite trend could ensue that is different from that shown in Figure 17.

5. CONCLUSIONS

We have considered two dominant micromechanisms of deformation in porous rocks, namely, crystal plasticity and microfracturing. Both micromechanisms initiate around the pores and propagate away from the pores in a way that depends strongly on the degree of brittleness of the material and the spatial distribution of the pores. The more brittle the material, the greater is the extent of damage from tensile loading. The pore-scale modeling conducted in this paper is a mechanistic way of understanding the smaller-scale processes responsible for the nucleation of macroscopic fractures and for explaining the origin of the fracture toughness of a given porous material.

For the combined shearing–extension simulations, we find that microfracturing produces a softer response than crystal plasticity. This is because the tensile stress that develops normal to the fracture plane necessitates the shear stress to be zero on that plane. Therefore, a stress drop is observed in the overall stress–strain curve. This is not the case with crystal plasticity, however, because the amount of shear stress in each crystallographic plane is bounded by the yield stress, and does not drop to zero even when slip systems activate. For quasi-brittle materials, it is expected that the micromechanisms of deformation will involve both ductile and brittle responses, with one type of response conceivably triggering the other. The overall stress–strain behavior is expected to be different when pores collapse and through-going fractures form. In general, these larger-scale processes will necessitate modeling beyond the range of the REV. Research along this line is underway.

ACKNOWLEDGEMENTS

This material is based upon work supported by the U.S. Department of Energy, Office of Science, Office of Basic Energy Sciences, Geosciences Research Program, under Award Number DE-FG02-03ER15454. The first author is grateful for a Stanford Graduate Fellowship and a John A. Blume Fellowship that provided partial support for his PhD studies at Stanford.

REFERENCES

1. Abousleiman YN, Hoang SK, Liu C. Anisotropic porothermoelastic solution and hydro-thermal effects on fracture width in hydraulic fracturing. *International Journal for Numerical and Analytical Methods in Geomechanics* 2014; **38**:493–597.
2. Arson C, Pereira JM. Influence of damage on pore size distribution and permeability of rocks. *International Journal for Numerical and Analytical Methods in Geomechanics* 2013; **37**:810–831.
3. Catalano E, Chareyre B, Barthélémy E. Pore-scale modeling of fluid-particles interaction and emerging poromechanical effects. *International Journal for Numerical and Analytical Methods in Geomechanics* 2014; **38**:51–71.
4. Foster CD, Nejad TM. Embedded discontinuity finite element modeling of fluid flow in fractured porous media. *Acta Geotechnica* 2013; **8**:49–57.
5. Fu P, Johnson SM, Carrigan C. An explicitly coupled hydro-geomechanical model for simulating hydraulic fracturing in arbitrary discrete fracture networks. *International Journal for Numerical and Analytical Methods in Geomechanics* 2013; **37**:2278–2300.
6. Ganzer L, Reitenbach V, Pudlo D, Albrecht D, Singhe AT, Awemo KN, Wienand J, Gaupp R. Experimental and numerical investigations on CO₂ injection and enhanced gas recovery effects in Altmark gas field (Central Germany). *Acta Geotechnica* 2014; **9**:39–47.
7. Gatuingt F, Snozzi L, Molinari JF. Numerical determination of the tensile response and the dissipated fracture energy of concrete: role of the mesostructure and influence of the loading rate. *International Journal for Numerical and Analytical Methods in Geomechanics* 2013; **37**:3112–3130.
8. Giwelli AA, Matsuki K, Sakaguchi K, Kizaki A. Effects of non-uniform traction and specimen height in the direct shear test on stress and deformation in a rock fracture. *International Journal for Numerical and Analytical Methods in Geomechanics* 2013; **37**:2186–2204.
9. Gou Y, Hou Z, Liu H, Zhou L, Were P. Numerical simulation of carbon dioxide injection for enhanced gas recovery (CO₂-EGR) in Altmark natural gas field. *Acta Geotechnica* 2014; **9**:49–58.
10. Huang K, Zhang Z, Ghassemi A. Modeling three-dimensional hydraulic fracture propagation using virtual multi-dimensional internal bonds. *International Journal for Numerical and Analytical Methods in Geomechanics* 2013; **37**:2021–2038.
11. Jourdain X, Colliat JB, De Sa C, Benboudjema F, Gatuingt F. Upscaling permeability for fractured concrete: meso?macro numerical approach coupled to strong discontinuities. *International Journal for Numerical and Analytical Methods in Geomechanics* 2014; **38**:536–550.
12. Katsuki D, Gutierrez M, Almrabat A. Stress-dependent elastic wave velocity of microfractured sandstone. *International Journal for Numerical and Analytical Methods in Geomechanics* 2014; **38**:441–456.
13. Lamb AR, Gorman GJ, Elsworth D. A fracture mapping and extended finite element scheme for coupled deformation and fluid flow in fractured porous media. *International Journal for Numerical and Analytical Methods in Geomechanics* 2013; **37**:2916–2936.
14. Li L, Meng Q, Wang S, Li G, Tang C. A numerical investigation of the hydraulic fracturing behaviour of conglomerate in Glutenite formation. *Acta Geotechnica* 2013; **8**:597–618.
15. Sarris E, Papanastasiou P. Numerical modeling of fluid-driven fractures in cohesive poroelastoplastic continuum. *International Journal for Numerical and Analytical Methods in Geomechanics* 2013; **37**:1822–1846.
16. Vallin V, Pereira JM, Fabbri A, Wong H. Numerical modelling of the hydro-chemo-mechanical behaviour of geomaterials in the context of CO₂ injection. *International Journal for Numerical and Analytical Methods in Geomechanics* 2013; **37**:3052–3069.
17. Vu M, Pouya A, Seyedi DM. Theoretical and numerical study of the steady-state flow through finite fractured porous media. *International Journal for Numerical and Analytical Methods in Geomechanics* 2013; **37**:221–235.
18. Vu M, Pouya A, Seyedi DM. Modelling of steady-state fluid flow in 3D fractured isotropic porous media: application to effective permeability calculation. *International Journal for Numerical and Analytical Methods in Geomechanics* 2013b; **37**:2257–2277.
19. Xu T, Xu Q, Tang C, Ranjith PG. The evolution of rock failure with discontinuities due to shear creep. *Acta Geotechnica* 2013; **8**:567–581.
20. Schöpfer MPJ, Childs C, Manzocchi T. Three-dimensional failure envelopes and the brittle-ductile transition. *Journal of Geophysical Research: Solid Earth* 2013; **118**:1378–1392.
21. Byerlee JD. Brittle-ductile transition in rocks. *Journal of Geophysical Research* 1968; **73**:4741–4750.
22. Mogi K. Pressure dependence of rock strength and transition from brittle fracture to ductile flow. *Bulletin Earthquake Research Institute Tokyo University* 1966; **44**:215–232.
23. Baud P, Schubnel A, Wong TF. Dilatancy, compaction and failure mode in Solnhofen limestone. *Journal of Geophysical Research* 2000; **105**:19289–19303.
24. Hirth G, Tullis J. The effects of pressure and porosity on the micromechanics of the brittle-ductile transition in quartzite. *Journal of Geophysical Research* 1989; **94**:17825–17838.
25. Zhang J, Wong TF, Davis DM. Micromechanics of pressure-induced grain crushing in porous rocks. *Journal of Geophysical Research* 1990; **95**:341–352.
26. Vajdova V, Zhu W, Chen TMN, Wong TF. Micromechanics of brittle faulting and cataclastic flow in Tavel limestone. *Journal of Structural Geology* 2010; **32**:1158–1169.

27. Vajdova V, Baud P, Wu L, Wong TF. Micromechanics of inelastic compaction in two allochemical limestones. *Journal of Structural Geology* 2012; **43**:100–117.
28. Li X, Hai-Sui Y, Li XS. A virtual experiment technique on the elementary behaviour of granular materials with discrete element method. *International Journal for Numerical and Analytical Methods in Geomechanics* 2013; **37**:75–96.
29. Wang B, Chen Y, Wong TF. A discrete element model for the development of compaction localization in granular rock. *Journal of Geophysical Research* 2008; **113**:B03202.
30. Wang J, Yan H. On the role of particle breakage in the shear failure behavior of granular soils by DEM. *International Journal for Numerical and Analytical Methods in Geomechanics* 2013; **37**:832–854.
31. Grujovic N, Divac D, Zivkovic M, Slavkovic R, Milivojevic N, Milivojevic V, Rakic D. An inelastic stress integration algorithm for a rock mass containing sets of discontinuities. *Acta Geotechnica* 2013; **8**:265–278.
32. Borja RI, Wren JR. Discrete micromechanics of elastoplastic crystals. *International Journal for Numerical Methods in Engineering* 1993; **36**:3815–3840.
33. Borja RI, Rahmani H. Computational aspects of elasto-plastic deformation in polycrystalline solids. *Journal of Applied Mechanics* 2012; **79**(031024). DOI: 10.1115/1.4005898.
34. Armero F, Garikipati K. An analysis of strong discontinuities in multiplicative finite strain plasticity and their relation with the numerical simulation of strain localization in solids. *International Journal of Solids and Structures* 1996; **33**:2863–2885.
35. Borja RI, Regueiro RA. Strain localization of frictional materials exhibiting displacement jumps. *Computer Methods in Applied Mechanics and Engineering* 2001; **190**:2555–2580.
36. Foster CD, Borja RI, Regueiro RA. Embedded strong discontinuity finite elements for fractured geomaterials with variable friction. *International Journal for Numerical Methods in Engineering* 2007; **72**:549–581.
37. Linder C, Armero F. Finite elements with embedded strong discontinuities for the modeling of failure in solids. *International Journal for Numerical Methods in Engineering* 2007; **72**:1391–1433.
38. Linder C, Rosato D, Miehe C. New finite elements with embedded strong discontinuities for the modeling of failure in electromechanical coupled solids. *Computer Methods in Applied Mechanics and Engineering* 2011; **200**:141–161.
39. Linder C, Raina A. A strong discontinuity approach on multiple levels to model solids at failure. *Computer Methods in Applied Mechanics and Engineering* 2013; **253**:558–583.
40. Mosler J, Meschke G. 3D modeling of strong discontinuities in elastoplastic solids: fixed and rotating localization formulations. *International Journal for Numerical Methods in Engineering* 2013; **5**:1553–1576.
41. Oliver X, Huespe AE. Continuum approach to material failure in strong discontinuity settings. *Computer Methods in Applied Mechanics and Engineering* 2004; **193**:3195–3220.
42. Simo JC, Oliver J. A new approach to the analysis and simulation of strain softening in solids. In *Fracture and Damage in Quasibrittle Structures*, ZP Bažant et al. (ed.). E&FN Spon: London, 1994; 25–39.
43. Price NJ, Cosgrove JW. *Analysis of Geological Structures*. Cambridge University Press: New York, 1990.
44. Baeta RD, Ashbee KHG. Mechanical deformation of quartz. *Philosophical Magazine* 1970; **22**:601–635.
45. McLaren AC, Retchford JA. Transmission electron microscope study of the dislocations in plastically deformed synthetic quartz. *Physica Status Solidi(a)* 1969; **33**:657–658.
46. Barber DJ, Wenk HR. Deformation twinning in calcite, dolomite, and other rhombohedral carbonates. *Physics and Chemistry of Minerals* 1979; **5**:141–165.
47. Ferrill DA, Morris AP, Evans MA, Burkhard M, Groshong, RH, Jr, Onasch CM. Calcite twin morphology: a low-temperature deformation geothermometer. *Journal of Structural Geology* 2004; **26**:1521–1529.
48. Mowar S, Zaman M, Stearns DW, Roegiers JC. Micro-mechanisms of pore collapse in limestone. *Journal of Petroleum Science and Engineering* 1996; **15**:221–235.
49. Pouya A. Micro-macro approach for the rock salt behaviour. *European Journal of Mechanics - A/Solids* 2000; **19**:1015–1028.
50. Borja RI. *Plasticity Modeling and Computation*. Springer-Verlag: Berlin, Heidelberg, 2013.
51. Bishop JFW, Hill R. A theory of the plastic distortion of a polycrystal aggregate under combined stress. *Philosophical Magazine* 1951; **42**:414–427.
52. Bishop JFW, Hill R. A theoretical derivation of the plastic properties of polycrystalline face-centered metal. *Philosophical Magazine* 1951; **42**:1298–1307.
53. Budiansky B, Wu TT. Theoretical prediction of plastic strains of polycrystals. In *Proceedings of the Fourth US National Congress on Applied Mechanics*, Rosenberg RM (ed.). ASME: New York, 1962; 1175–1185.
54. Hutchinson JW. Elastic-plastic behavior of polycrystalline metals and composites. *Proceedings of the Royal Society of London A* 1970; **319**:247–272.
55. Anand L, Kothari M. A computational procedure for rate-independent crystal plasticity. *Journal of the Mechanics and Physics of Solids* 1996; **44**:525–558.
56. Miehe C, Schröder J. A comparative study of stress update algorithms for rate-independent and rate-dependent crystal plasticity. *International Journal for Numerical Methods in Engineering* 2001; **50**:273–298.
57. Schröder J, Miehe C. Aspects of computational rate-independent crystal plasticity. *Computational Materials Science* 1997; **9**:168–176.
58. Izadbakhsh A, Inal K, Mishra RK. Crystal plasticity based finite element modelling of large strain deformation in AM30 magnesium alloy. *Modelling Sand Simulation in Materials Science and Engineering* 2012; **20**(035016). DOI: 10.1088/0965-0393/20/3/035016.

59. Ortiz M, Repetto EA, Stainier L. A theory of subgrain dislocation structures. *Journal of the Mechanics and Physics of Solids* 2000; **48**:2077–2114.
60. Steinmann P, Stein E. On the numerical treatment and analysis of finite deformation ductile single crystal plasticity. *Computer Methods in Applied Mechanics and Engineering* 1996; **129**:235–254.
61. Nemat-Nasser S, Obata M. Rate-dependent finite elastic-plastic deformation of polycrystals. *Proceedings of the Royal Society of London A* 1986; **407**:343–375.
62. Pan J, Rice JR. Rate sensitivity of plastic flow and implications for yield surface vertices. *International Journal of Solids and Structures* 1983; **19**:973–987.
63. Dumoulin S, Hopperstad OS, Berstad T. Investigation of integration algorithms for rate-dependent crystal plasticity using explicit finite element codes. *Computational Materials Science* 2009; **46**:785–799.
64. Ling X, Horstemeyer MF, Potirniche GP. On the numerical implementation of 3D rate-dependent single crystal plasticity formulations. *International Journal for Numerical Methods in Engineering* 2005; **63**:548–568.
65. Borja RI, Rahmani H. Discrete micromechanics of elastoplastic crystals in the finite deformation range. *Computer Methods in Applied Mechanics and Engineering* 2014; **275**:234–263.
66. Fossen H. Structural Geology Cambridge University Press. *New York* 2010:205–207.
67. Koiter WT. Stress-strain relations, uniqueness and variational theorems for elastic-plastic materials with a singular yield surface. *Quarterly Applied Mathematics* 1957; **11**:350–354.
68. Chambon R, Caillerie D, Viggiani G. Loss of uniqueness and bifurcation vs instability: some remarks. *Failure, Degradation and Instabilities* 2004:517–535.
69. Linder C, Zhang X. A marching cubes based failure surface propagation concept for three-dimensional finite elements with non-planar embedded strong discontinuities of higher-order kinematics. *International Journal for Numerical Methods in Engineering* 2013; **96**:339–372.
70. Linder C, Zhang X. Three-dimensional finite elements with embedded strong discontinuities to model failure in electromechanical coupled materials. *Computer Methods in Applied Mechanics and Engineering* 2014; **273**:143–160.
71. Borja RI. Bifurcation of elastoplastic solids to shear band mode at finite strain. *Computer Methods in Applied Mechanics and Engineering* 2002; **191**:5287–5314.
72. Mohammadnejad T, Khoei AR. Hydro-mechanical modeling of cohesive crack propagation in multiphase porous media using the extended finite element method. *International Journal for Numerical and Analytical Methods in Geomechanics* 2013; **37**:1241–1279.
73. Belytschko T, Black T. Elastic crack growth in finite elements with minimal remeshing. *International Journal for Numerical Methods in Engineering* 1999; **45**:601–620.
74. Borja RI. Assumed enhanced strain and the extended finite element methods: a unification of concepts. *Computer Methods in Applied Mechanics and Engineering* 2008; **197**:2789–2803.
75. Hughes TJR. *The Finite Element Method*. Prentice-Hall: New Jersey, 1987.
76. Duriez J, Darve F, Donzé F-V. Incrementally non-linear plasticity applied to rock joint modeling. *International Journal for Numerical and Analytical Methods in Geomechanics* 2013; **37**:453–477.
77. Liu F, Borja RI. Extended finite element framework for fault rupture dynamics including bulk plasticity. *International Journal for Numerical and Analytical Methods in Geomechanics* 2013; **37**:3087–3111.
78. Ball A, Payne BW. The tensile fracture of quartz crystals. *Journal of Materials Science* 1976; **11**:731–740.
79. Doukhan JC, Henry JP, Paquet J. Microstructure and brittle behavior of fine grain calcite (micrite). *Journal of Materials Science* 1976; **11**:1884–1892.
80. Vermeer PA, de Borst R. Non-associated plasticity for soils, concrete and rock. *Heron* 1984; **29**:1–64.
81. Oates JAH. *Lime and Limestone: Chemistry and Technology, Production and Uses*. Wiley-VCH: Weinheim, Germany, 1998.
82. He Z, Caratini G, Dormieux L, Kondo D. Homogenization of anisotropic elastoplastic behaviors of a porous polycrystal with interface effects. *International Journal for Numerical and Analytical Methods in Geomechanics* 2013; **37**:3213–3236.
83. Schmid E, Boas W. *Plasticity of Crystals with Special Reference to Metals, Translation from: Kristallplastizität mit besonderer Berücksichtigung der Metalle*. F.A, Hughes & Co.: London, 1935.